Journal of the European Ceramic Society xxx (xxxx) xxx–xxx

Contents lists available at ScienceDirect

Journal of the European Ceramic Society

journal homepage: www.elsevier.com/locate/jeurceramsoc

Original Article

# Anisotropic magnetic property and exchange bias effect in a homogeneous Sillen-Aurivillius layered oxide

Zezhi Chen[a], Tao Hong[b], Zhenbin Wang[c], Jianlin Wang[d,e], Haoliang Huang[d,e], Ranran Peng[a,d,f,*], Wensheng Yan[d,e], Zhengping Fu[a,d,f], Kyle S. Brinkman[g], Yalin Lu[a,d,e,f,*]

[a] CAS Key Laboratory of Materials for Energy Conversion, Department of Materials Science and Engineering, University of Science and Technology of China, Hefei, 230026, PR China
[b] School of Materials Science and Engineering, Hefei University of Technology, Hefei, 230009, PR China
[c] Department of Nano Engineering, University of California, San Diego, 9500 Gilman Drive, La Jolla, California, 92093-0448, United States
[d] Quantum Materials & Photonic Technology Laboratory, Synergetic Innovation Center of Quantum Information & Quantum Physics, University of Science and Technology of China, Hefei, 230026, PR China
[e] National Synchrotron Radiation Laboratory, University of Science and Technology of China, Hefei, 230026, PR China
[f] Hefei National Laboratory for Physical Sciences at the Microscale, University of Science and Technology of China, Hefei, 230026, PR China
[g] Department of Materials Science and Engineering, Clemson University, Clemson, SC, 29634, United States

ARTICLE INFO

*Keywords:*
Sillen-Aurivillius
Oriented ceramic
Exchange bias
Magnetic anisotropy
Spin glass

ABSTRACT

A new Sillen-Aurivillius oxide $Bi_7Fe_2Ti_2O_{17}Cl$ (BFTOCl), in which four perovskite layers are sandwiched by Sillen slabs, is designed and prepared by the solid-state reaction. Compared with pure Aurivilius structure, the Sillen slab requires one less positive charge for charge compensation due to the intercalation of Cl anions between two $(Bi_2O_2)^{2+}$, which increases the concentration of magnetic $Fe^{3+}$ ions in perovskite slab, and may depress the interaction of $Fe^{3+}$ ions existing in neighboring perovskite slabs. This unique natural superlattice structure and the highly orientated texture of the ceramic result in a complex spin structure and an interesting magnetic anisotropy. The magnetism in in-plane direction (0.00487 emu/g at 100 K) is about 2.5 times larger than that in out-of-plane direction. Remarkably, exchange bias anisotropy has been observed in the BFTOCl ceramic, of which the exchange bias fields in in-plane and out-of-plane directions are 345 and 174 Oe at 100 K, respectively.

## 1. Introduction

Spintronics concerns the intrinsic spin of electrons and the associated magnetic moments. This field has drawn special attention due to a number of important fundamental science questions and also offers opportunities to realize novel phenomena and contribute to emerging applications in quantum devices. [1–3] In spintronic devices, the exchange bias (EB) effect is the fundamental magnetic interaction used to control the spin flip. This effect utilizes the coupling between ferromagnetic (FM) and antiferromagnetic (AFM) bilayers, and thus has wide potential applications in spin valves, [4] magnetic random access memories (MRAMs) [5], and hard drive reading heads [6]. In general, the EB effect is achieved from the suppressed flip of FM spins that are coupled to the AFM layers, resulting in a hysteresis loop of the FM, which is shifted along the field axis. As an interfacial phenomenon, the EB effect has been extensively studied in multi-film systems, core-shell nanoparticles and other artificial materials with heterogeneous magnetic regions [7–12]. Although many efforts [6,13,14] have been made to improve the EB properties, tailoring the coupling of magnetism at the AFM/FM interface is a key challenge to achieve better spintronics [15].

Recently, the EB effect has been realized in single-phase materials containing AFM and FM interactions within a homogeneous structure. For example, $YbFe_2O_4$ possessing two magnetic sublattices [16], a $SmFeO_3$ single crystal with a FM background and AFM clusters, [17] $BiFeO_3$ nanocrystals [18] having a native core (AFM) / shell (spin-cluster) structure, $Ba_2FeOs_{0.88}O_6$ [19] and Heusler alloys [20] with compensated ferrimagnetism in a ferromagnet. The findings in these materials systems transcend the restricted AFM/FM interface of the traditional heterogeneous EB material systems and may contribute to better magnetic coupling and excite new interest in terms of both basic science and potential applications. For example, using a single-phase EB material to substitute for the AFM/FM bilayer, better device integration can be achieved in spin valve and magnetic tunnel junction devices as shown in Fig. S1 (a) and (b) (in Electronic Annex). Moreover, if an EB anisotropy can be realized in single phase materials, new functionality may be revealed as illustrated in Fig. S1 (c), of which the different

* Corresponding authors at: Department of Materials Science & Engineering, University of Science and Technology of China, Hefei, 230026, PR China.
*E-mail addresses:* pengrr@ustc.edu.cn (R. Peng), yllu@ustc.edu.cn (Y. Lu).

https://doi.org/10.1016/j.jeurceramsoc.2019.03.006
Received 20 November 2018; Received in revised form 22 February 2019; Accepted 1 March 2019

crystal orientations (such as in-plane and out-of-plane directions) possessing different degree of pinning effects can be used as free and pinned FM layers, respectively. Simultaneously, the free and pinned FM layers can be switched relative to each other, with the change of the magnetic field direction which may result in a new modulation factor for enhanced spintronics. Unfortunately, the EB effect in existing single-phase materials usually vanishes or is small at the room temperature, and no naturally occurred single-phase EB anisotropy has been reported to date in existing literature.

Very recently, we found that single-phase, long-period Aurivillius oxides with the formula of $Bi_{n+1}Fe_{n-3}Ti_3O_{3n+3}$ ($(Bi_2O_2)^{2+}$-$(Bi_{n-1}Fe_{n-3}Ti_3O_{3n+1})^{2-}$), where $n$ indicates the number of perovskite layers, possess a good EB effect due to the coupling between the inside AFM layers and spin glass (SG) when $n \geq 7$ [29–32]. Moreover, the block temperatures (the highest existing temperature) for the EB effect increase with the number of perovskite layers ($n$) due to the enhanced concentration of magnetic ions embedded in the perovskite slabs. Nevertheless, the RT EB effect cannot be achieved by simply increasing the perovskite layer in these Aurivillius oxides due to their close Gibbs free energies when $n \geq 10$, which makes it difficult to obtain homogeneous Aurivillius oxides. [24–26] Therefore, efforts on finding novel materials or new functional mechanisms is of key importance in order to realize desirable RT EB in single-phase materials.

Sillen − Aurivillius oxides have very similar structures to Aurivillius oxides and can be described as $(Bi_2O_2XBi_2O_2)^{3+}$ $(A_{n-1}B_nO_{3n+1})^{3-}$ ($X$ = F, Cl, Br). Compared to pure Aurivillius oxides, the existence of a Sillen layer can effectively reduce the total valence of the $B$ site (Fe-Ti) and thus improve the content of magnetic ions (Fe) in the perovskite slab with the same layer number ($n$). To develop a potential RT EB material, a new compound with the formula of $Bi_7Fe_2Ti_2O_{17}Cl$ (BFTOCl, $n = 4$) was designed in this work. The resulting materials form a homogenous structure (in Fig. 1(a)) which has been theoretically and experimentally investigated. The as-prepared BFTOCl ceramic was shown to exhibit two spin-glass-like behaviors, and their origins, which may contribute to the understanding of complex magnetism in layer-structured oxides, have been discussed. Moreover, the BFTOCl ceramic demonstrates an obvious large EB anisotropy. To the best of our knowledge, this is the first time such a phenomenon has been observed in a single-phase material, which results in a new regulation factor for spin flipping. Significantly, the RT EB effect has been successfully realized with this new compound, which is even superior to 9-layer ($n = 9$) Aurivillius oxides. [21] These findings shed new light on single-phase anisotropic EB materials and on provide a basis for further study of the underlying mechanisms.

## 2. Experimental section

### 2.1. Sample preparation

$Bi_7Fe_2Ti_2O_{17}Cl$ (BFTOCl) ceramics are prepared via a conventional solid-state reaction technique. The detailed synthesis conditions and procedures are as follows: first, appropriate amounts of the $Bi_2O_3$, $Fe_2O_3$, $TiO_2$, BiOCl raw materials are ball milled in ethanol for 48 h. Next, the mixture is dried and then calcined at 770 °C for 5 h to obtain BFTOCl powders. BFTOCl powders are pressed into pellets with a diameter of 25 mm and a thickness of 5 mm. Finally, the pellets are sintered at 820 °C for 4 h under a pressure of 10 MPa in a hot-press sintering furnace (Materials Research Furnaces Inc., Suncook, NH, USA) under an atmosphere of mixed Ar/$O_2$ gas.

### 2.2. Computational method

All spin-polarized density functional theory (DFT) calculations were performed using the Vienna ab initio simulation package (VASP) within the projected-augmented wave method. [27,27] The Perdew-Burke-Ernzerhof (PBE) functional with a Hubbard U value of 5.3 eV for Fe was used. [28–30] The energy cutoff was 520 eV. The electronic energy and atomic force were smaller than 1e-5 eV and 0.01 eV/Å, respectively. The 4 × 4 × 1 k-point mesh was adopted for the Brillouin zone integration of the $Bi_7Fe_2Ti_2O_{17}Cl$ unit cell.

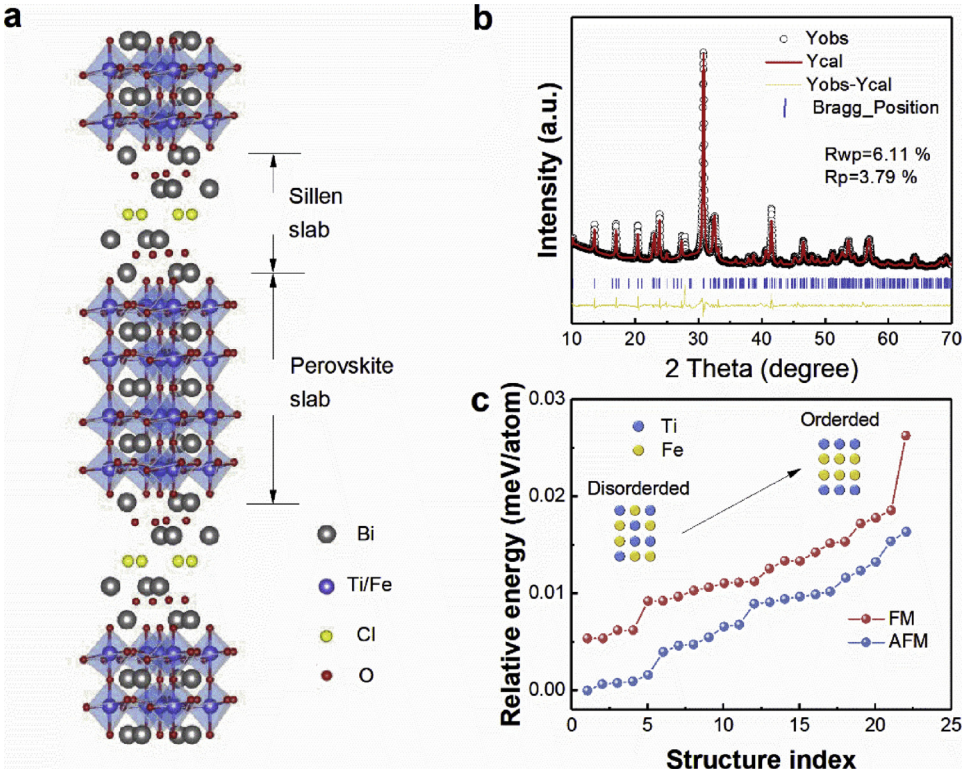


**Fig. 1.** (a) Modified Sillen-Aurivillius structure with 4-layers perovskite ($Bi_7Fe_2Ti_2O_{17}Cl$); (b) Rietveld refinement of the BFTOCl powders; (c) Relative total energies of 22 symmetrically distinct structures of the unit cell $Bi_7Fe_2Ti_2O_{17}Cl$, with Fe ions in FM (red) and AFM (blue) states. The energy of the lowest-energy structure was set as the zero reference.

### 2.3. Characterization techniques

The crystalline structure of samples is investigated using an X-ray diffractometer (Rigaku TTR III, Tokyo, Japan) employing Cu $K_{\alpha 1}$ radiation ($\lambda$ = 1.5406 Å). The atomic structure is visualized using the aberration-corrected scanning transmission electron microscopy high-angle annular dark field (HAADF-STEM) and selected area electron diffraction (SAED) (JEM-ARM200 F; JEOL, Akishima-shi, Japan). The line-scanning of elements analysis is performed on the equipped X-ray energy dispersive spectroscopy (EDS) (X-max80, Oxford Instruments). The fracture surface of the ceramic is imaged via scanning electron microscopy (SEM; JSM-6390LA, JEOL, Akisshima-shi, Japan). The TEM images are obtained using a Hitachi HT7650 microscope (TEM; JSM-7650, JEOL, Akisshima-shi, Japan) operated at 100 kV. The orientations of the individual grains on the surface of the samples are obtained using electron-backscattered diffraction (EBSD). The EBSD measurement was obtained using a scanning electron microscope (SEM) (Hitachi S-6600) equipped with field emission. A high-speed DigiView CCD camera was used for pattern acquisition, and data were recorded using a 50 nm step size. The magnetic properties of the samples are characterized using a vibrating samples magnetometer (VSM, Quantum Design Inc., San Diego, CA, USA). The soft X-ray absorption spectra (XAS) are collected on the BL12B-a of the National Synchrotron Radiation Laboratory (NSRL, Hefei, P. R. China) using the synchrotron radiation from the storage ring running at 800 MeV with an average current of 300 mA. The XMCD measurements are performed at the beamline 08U-a in the Shanghai Synchrotron Radiation Facility in Shanghai, P. R. China.

## 3. Results and discussions

### 3.1. Structure characterization

The BFTOCl powders with designed composition were prepared using the conventional solid phase reaction and calcined at 770 °C for 5 h. Fig. 1(a) presents the crystal structure of BFTOCl that was constructed by inserting $BiFeO_3$ into $Bi_6FeTi_2O_{14}Cl$ structures, with Fe/Ti equivalently occupying the same site. Utilizing this artificial structure, we performed the XRD Rietveld refinement for the BFTOCl powders, as shown in Fig. 1(b) resulting in $R_{wp}$ and $R_p$ values of 6.11% and 3.79%, respectively. The low $R_{wp}$ and $R_p$ indices and the fitted peaks reflect close agreement with the predicted structure, which corresponds to an orthorhombic structure (space group P nc2) with lattice parameters of $a$ = 0.5496 ± 0.0001 nm, $b$ = 0.5531 ± 0.0001 nm and $c$ = 2.6072 ± 0.0001 nm. To identify the magnetic round state of Fe ions, we performed DFT calculations for BFTOCl with Fe ions in both FM and AFM states. Fig. 1(c) shows the relative energies of 22 symmetrically distinct ordered structures with Fe ions in FM states and AFM states. We observed that the disordered structures of BFTOCl with Fe ions in the AFM state have a relatively lower energy than those of Fe ions in the FM state, suggesting that the ground state of Fe ions in BFTOCl is the AFM state, which is similar to that in Aurivillius oxides. [31–33] Additionally, the trivial energy difference (15 meV/atom) of the 22 ordered AFM BFTOCl structures indicates that BFTOCl tends to be disordered at elevated temperatures, which is consistent with our previous XRD results.

HAADF-STEM was used to visualize the atomic structure of BFTOCl powders. As shown in Fig. 2, an orderly arrangement of bright spots can be clearly observed. The intensity of the spots in a HAADF-STEM image that is approximately proportional to the square of the atomic number (Z) of the ions. The bright spots shown in Fig. 2 should correspond to Bi atoms. As shown in Fig. 2(a), the visual structure of BFTOCl agrees well with the designed one (Fig. 1(a)) with perovskite slabs ($n$ = 4) and Sillen block alternately stacked, indicating the high quality of the obtained sample. Selected area electron diffraction (SAED) patterns obtained from the HAADF image of the (100) plane confirm the long-range periodic structure and the good crystallinity of the BFTOCl powders. The EDS results show that the element ratio is relatively close to the nominal composition as shown in Fig. S2.

Fig. 2(b) and (c) shows enlarged HAADF-STEM images of the BFTOCl (110) and (100) planes, from which the atomic distance can be measured. The measured values are in good accordance with the simulated lattice parameters. Moreover, Fig. 2(b) and (c) jointly indicates that the distribution of the Bi layers in the perovskite is not uniform along the [001] direction as illustrated in Fig. 2(d). This finding should be ascribed to the impact from the Sillen block, similar to the previous reports on Aurivillius oxide, for which a longer distance is observed for the Bi-Bi layers that are adjacent to the fluorite-like layers (0.44 nm in middle, 0.49 nm in side). [34,35] Notably, the large difference in Bi-Bi the distances along the [100] and [001] directions within the perovskite slab strongly indicates the complicated structural distortions with compressive strain in the in-plane direction ([100] and [010] direction). This distortion is due to close packing of the Bi ions in the Sillen slab, which may induce magnetic anisotropy changes, as suggested in several material systems, such as $La_{0.7}Sr_{0.3}MnO_3$ [36], $SrRuO_3$ [37] and $La_2CoMnO_6$ [38]. The natural superlattice structure in BFTOCl may also result in some fantastic magnetic properties, similar to those in heterogeneous superlattice films [39].

### 3.2. Characterization of the BFTOCl ceramic

Fig. 3(a) shows the SEM image of the cross section and surface of the BFTOCl ceramic that was sintered at 820 °C for 4 h under the pressure of 10 MPa in a hot-press sintering furnace. Small pores can be detected in the BFTOCl ceramic, indicating that the ceramic is fairly dense. The BFTOCl sheets can be obviously observed in Fig. 3(a) and Fig. S3, indicating the preferential growth orientation. Electron backscattered diffraction (EBSD) mapping is employed to investigate the sample's orientation, for which the BFTOCl ceramic surface is polished before characterization. As shown in Fig. 3(b), the blue regions obviously dominate the surface area, indicating that the ceramic surface mostly consists of the (00$l$) orientation.

The XRD pattern of the BFTOCl ceramic shows a strong orientation, as demonstrated by the largely enhanced (0 0 $l$) peak intensities in Fig. 4. To quantitatively analyze the degree of orientation, the Lotgering method is applied using Eqs. (1)–(3) [40]:

$$P = \frac{\sum I(00l)}{\sum I(hkl)} \tag{1}$$

$$P_0 = \frac{\sum I_0(00l)}{\sum I_0(hkl)} \tag{2}$$

$$f_{(00l)} = \frac{P - P_0}{1 - P_0} \tag{3}$$

where $I(hkl)$ and $I_0(hkl)$ are the peak intensities of the ($hkl$) plane in the ceramic and powder samples, respectively; $P$ and $P_0$ are the ratios of all (0 0 $l$) (l = 1, 2, 3…) peak densities to the total peak densities in the ceramic and powders, respectively; and $f_{(0\ 0\ l)}$ indicates the Lotgering factor in the (0 0 $l$) planes. Here, $f_{(0\ 0\ l)}$ is calculated as 72.2%, suggesting that the sintered ceramic is mainly oriented in the (00 l) orientation. This result agrees well with the EBSD result.

### 3.3. Magnetic characterizations

Considering the primarily $c$-axis orientation and the obvious lattice distortion, as previously discussed, the magnetic anisotropy of the BFTOCl ceramic is investigated for the magnetic field being applied in different directions. As shown in Fig. 5(a), the in-plane, out-of-plane and sloping-plane directions indicate that the ceramic surface was parallel, perpendicular and at a 45° deviation angle to the applied field, respectively. The zero-field-cooled (ZFC) and field-cooled (FC) magnetizations measured in the different directions are shown in Fig. 5(b).

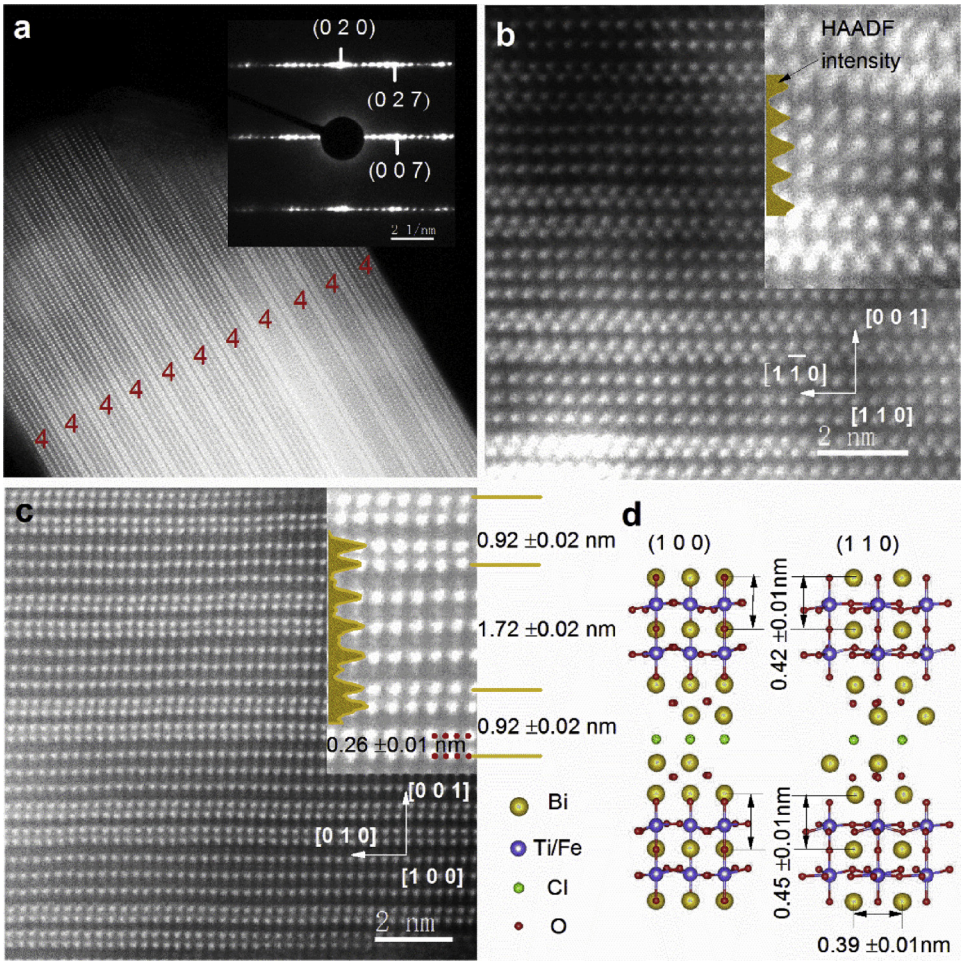


**Fig. 2.** (a) HAADF-STEM images of BFTOCl powder with its selected area electron diffraction (SAED) patterns. HAADF-STEM images of (b) (110) and (c) (100) planes for BFTOCl powders. The inserts show the intensities of spots in the HAADF image for the measurements of the Bi-Bi layer distance. (d) The sketch map of the BFTOCl structure with the data obtained from (b) and (c).

The bifurcation temperature for the FC and ZFC curves, which are higher than that at room temperature, indicates the onset of a weak FM state. [41] Below the bifurcation temperature, the irreversibility between the ZFC and FC curves reflects the appearance of the uncompensated electron spin, which comes from the $Fe^{3+}$ ions as confirmed by the XMCD results shown in Fig. S4 and S5. Both the ZFC and FC curves rise significantly as the temperature is lowered, which is ascribed to the paramagnetic magnetic effect from isolated Fe ions. [22] A similar phenomenon has also been observed in Aurivillius oxide $Bi_7Fe_3Ti_3O_{21}$, which has the same Fe ion concentration in the perovskite slab as BFTOCl, as shown in Fig. S6.

Interestingly, two broad peaks were observed in the ZFC curve in the in-plane direction, for which the intensity of the low-temperature peak is much larger than that of the high-temperature one. The large temperature gap between the two peaks (peak temperatures ($T_f$) of 70 and 173 K, respectively) clearly suggests the existence of two functional mechanisms. As shown in Fig. S7, the AC susceptibility measurement indicates that both peak temperatures, denoted as $T_{fI}$ and $T_{fII}$, shift toward higher temperatures at higher frequencies, strongly suggesting two magnetic glass-like behaviors [41]. Unlike those in nanoparticles [42] or nanobelts [23], such twin glass-like behaviors are seldom observed in ceramic samples due to their large grain size which depresses

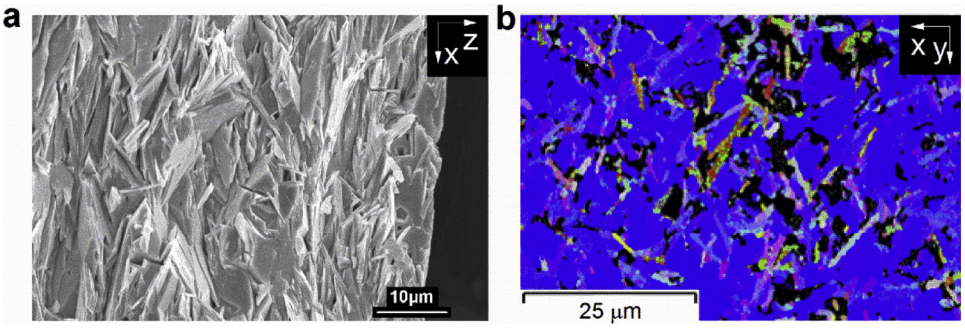


**Fig. 3.** (a) Cross section SEM image of the BFTOCl ceramic (indicated as xz plane). (b) Ceramic surface (indicated as xy plane) EBSD maps are obtained in different orientations denoted by the different colors: the red, green and blue colors represent the (100), (010) and (001) orientations, respectively.

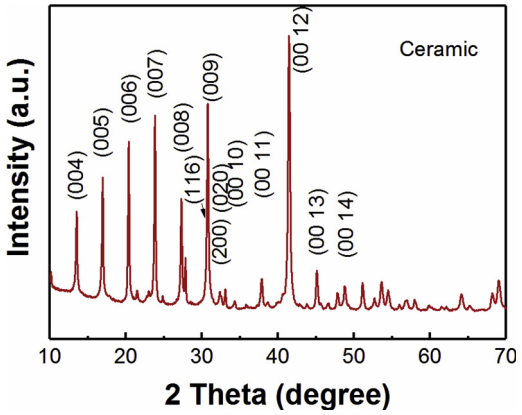


**Fig. 4.** The XRD pattern of BFTOCl ceramic surface.

surface effects including the uncompensated surface spins. Moreover, the high-temperature peak depends greatly on the direction of the applied filed. This peak also appears in the sloping-plane direction, however it disappears when measured in the out-of-plane direction. Different magnetic fields were used to further investigate the ZFC and FC curves, as shown in Fig. S8. The reduction in $T_{fI}$ and $T_{fII}$ in the ZFC curves for the enhanced magnetic field, as summarized in Table S1 (in Electronic Annex), further confirms their glass-like behaviors [43]. Based on the magnetic anisotropy and the glass-like behaviors, the *fI* and *fII* peaks in the FC and ZFC curves represent the AFM domain wall pinning effect from adjacent domains and the SG within the domains, respectively (detailed analyses in Electronic Annex).

Magnetic hysteresis (MH) loops measured in the in-plane and out-of-plane directions are shown in Fig. S10, and their related coercivity ($H_c$) and remnant magnetization ($M_r$) values are shown in Fig. 5(c) and (d). The values of $M_r$ and $H_c$ in the in-plane direction are both larger than those in the out-of-plane direction, presenting obvious magnetic anisotropy due to the blocking effect of the Sillen slab and the strong orientation in the BFTOCl ceramic. Moreover, at $T_{fI}$ and $T_{fII}$, the values of $H_c$ and $M_r$ are both in the valley position, as shown in Fig. 5(c) and (d). As mentioned above, spins tend to be regularly arranged as the temperature decreases. This means that AFM interaction tends to reduce the magnetism and FM has the opposite effect, which result in the broad freezing peaks on ZFC curve. Consequently, the net magnetic moment is easy to change with the measuring magnetic field at freezing peaks, which means that smaller $H_c$ and $M_r$ are observed in the hysteresis loop measurement due to the easier flip of spins. A similar phenomenon has also been observed in nanocrystalline $BiFeO_3$ [44]. Interestingly, the magnetic anisotropy in the two planes can be retained even above room temperatures, suggesting that this ceramic has a high Curie temperature.

### 3.4. Exchange bias

As previously mentioned, the BFTOCl presents complex magnetic behaviors, which greatly depend on the measured temperature and the direction and strength of the applied field. Considering the coexistence of AFM, FM, SG, and the domain wall pinning effect, the BFTOCl potentially exhibits the EB effect. As shown in Fig. S11, obvious shifts along the axis can be observed for the BFTOCl ceramics measured in both directions, demonstrating the presence of the EB effect. The magnitude of the observed EB effect can be characterized by the exchange bias field ($H_{EB}$), as defined in the Eq. (4):

$$H_{EB} = |H_1 + H_2| \quad (4)$$

where $H_1$ and $H_2$ are the left and right coercive fields, respectively. To avoid false signals due to a lack of saturation [45], a magnetic field that is much larger than the coercive field are used to measure the *MH* curves. The authenticity of the EB effect is also reflected in the measurement with a small FC process, as shown in Fig. S12, in which the differences in $H_E$ between both directions are not obvious at temperatures below $T_{fI}$. This result may be due to the pinning effect of domain walls on the flips of the spins, which has no anisotropy. Such a pinning effect can also explain the similar trough temperature of the EB valley to $T_{fI}$ measured in both directions.

The obvious distinction in the $H_{EB}$ values measured in the in-plane

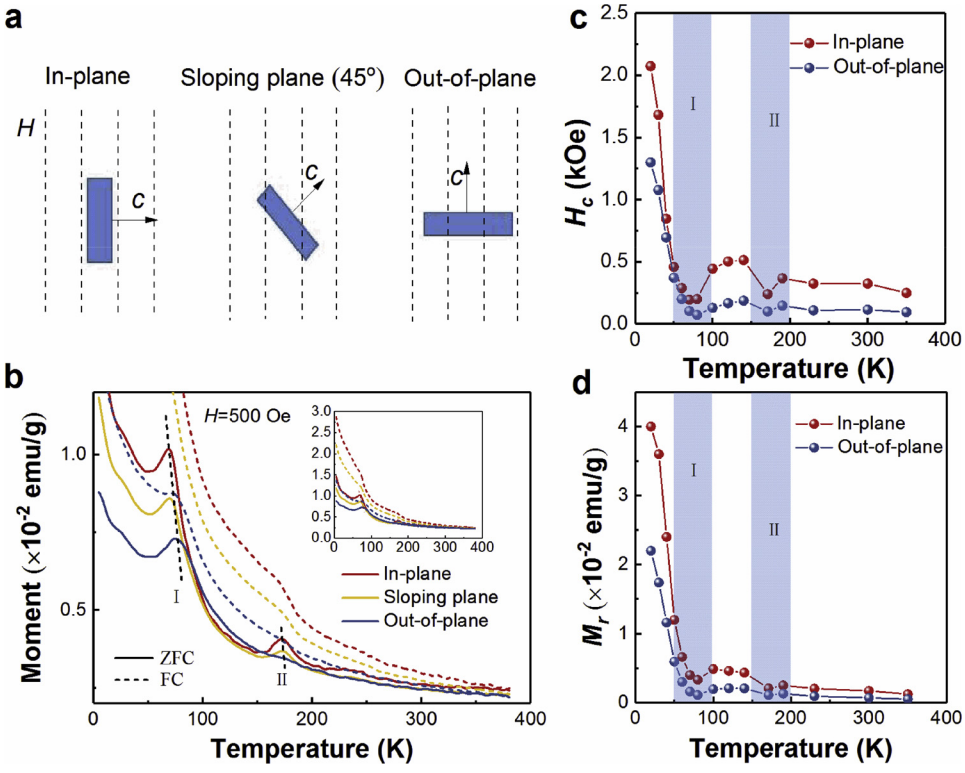


**Fig. 5.** (a) Relative directions between the samples and the magnetic field for the magnetic measurements. (b) The ZFC and FC curves for the in-plane, out-of-plane and sloping plane (45° with the field directions) directions, and the illustration compares the complete ZFC and curves. (c) and (d) Temperature dependence of the coercive field ($H_c$) and remanence ($M_r$) for the in-plane and out-of-plane directions.

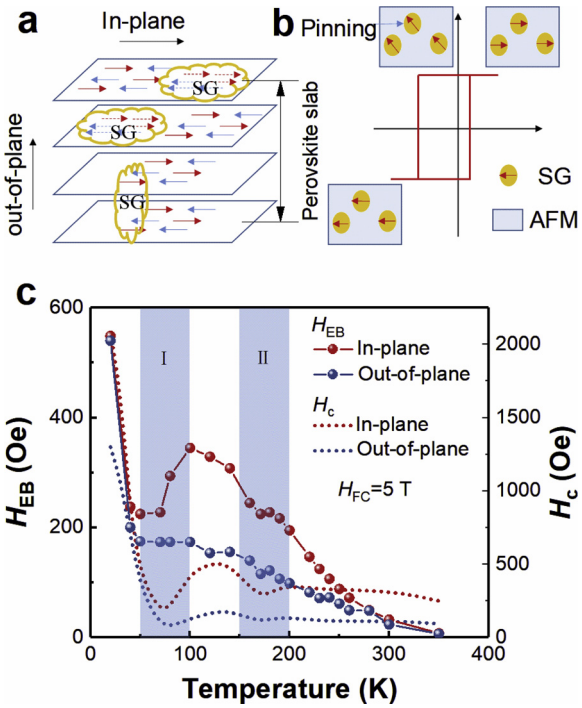


**Fig. 6.** (a) and (b) illustration of the EB effect in BFTOCl. (c) Exchange field of BFTOCl measured in the in-plane and out-of-plane directions at various temperatures.

and out-of-plane directions can be observed in the temperature range of 50–270 K, for which the domain wall pinning effect disappears, suggesting the anisotropy of the EB effect. This is also the first observation of such an anisotropy of the EB effect in a single-phase material. This difference can be attributed to the parallel direction of the dominant spins and the in-plane applied field after the FC process. As shown in Fig. 6(a), after the field cooling process, the frustrated spins tend to be parallel to the applied magnetic field. For the in-plane test, the in-plane uncompensated AFM spins couple with the SG spins as a torque on these SG spins to work to maintain the SG spins aligned along the direction of the cooling field and suppress the SG spins from flipping when the applied magnetic field changes to the opposite direction of the cooling field, as illustrated in Fig. 6(b). In the case of the out-of-plane field cooling, it would be difficult for the AFM to freeze the out-of-plane-oriented spin due to the lack of a long-range AFM magnetic interaction, thus resulting in lower $H_{EB}$ values. Notably, the EB effect with a $H_{EB}$ value of approximately 30 Oe can be detected when measured in both directions even at RT, which successfully fulfills our desire to develop a room-temperature single-phase EB material.

## 4. Conclusions

In summary, a new single-phase layer-structured oxide (BFTOCl) with a RT EB effect has been developed. The intercalation of Cl ions increases the thickness of the Sillen slab and the concentration of magnetic ions. Two freezing processes were observed in this complex magnetic system, originating from the blocked SG spin and the domain wall pinning effect, separately. Obvious magnetic and exchange bias anisotropy has been observed in the BFTOCl ceramic, which should be based on the natural superlattice-like structure and the complex magnetic interactions in BFTOCl. Our findings give an informative understanding of the origin of the EB effect in single-phase materials and suggest a new system of materials for use in future applications based on the EB effect.

## Conflicts of interest

There are no conflicts to declare.

## Acknowledgements

This work is supported by the National Key R&D Program of China (2016YFA0401004), the Chinese Universities Scientific Fund (CUSF, WK2310000055), Anhui Provincial Natural Science Foundation (P. R. China, No. 1608085QE91), and the External Cooperation Program of BIC (Chinese Academy of Sciences, No. 211134KYSB20130017). XAS and XMCD measurements were performed at the beamline BL12B-a in the National Synchrotron Radiation Laboratory (NSRL) in Hefei and the beamline 08U-a in the Shanghai Synchrotron Radiation Facility in Shanghai, P. R. China, respectively. We acknowledge the Supercomputing Center of University of Science and Technology of China (USTC) for providing computational resources.

## Appendix A. Supplementary data

Supplementary material related to this article can be found, in the online version, at doi:https://doi.org/10.1016/j.jeurceramsoc.2019.03.006.

## References

[1] M. Eschrig, Spin-polarized supercurrents for spintronics: a review of current progress, Rep. Prog. Phys. 78 (2015) 104501, https://doi.org/10.1088/0034-4885/78/10/104501.
[2] S. Bhatti, R. Sbiaa, A. Hirohata, H. Ohno, S. Fukami, S.N. Piramanayagam, Spintronics based random access memory: a review, Mater. Today 20 (2017) 530–548, https://doi.org/10.1016/j.mattod.2017.07.007.
[3] K. Schlage, L. Bocklage, D. Erb, J. Comfort, H.-C. Wille, R. Röhlsberger, Spin-Structured Multilayers: A New Class of Materials for Precision Spintronics, Adv. Funct. Mater. 26 (2016) 7423–7430, https://doi.org/10.1002/adfm.201603191.
[4] J.C.S. Kools, Exchange-biased spin-valves for magnetic storage, IEEE Trans. Magn. 32 (1996) 3165–3184, https://doi.org/10.1109/20.508381.
[5] A.D. Kent, D.C. Worledge, A new spin on magnetic memories, Nat. Nanotechnol. 10 (2015) 187–191, https://doi.org/10.1038/nnano.2015.24.
[6] B. Dieny, V.S. Speriosu, S.S.P. Parkin, B.A. Gurney, D.R. Wilhoit, D. Mauri, Giant magnetoresistive in soft ferromagnetic multilayers, Phys. Rev. B 43 (1991) 1297–1300, https://doi.org/10.1103/PhysRevB.43.1297.
[7] Z. Liu, M.D. Biegalski, S.-L. Hsu, S. Shang, C. Marker, J. Liu, L. Li, L. Fan, T.L. Meyer, A.T. Wong, J.A. Nichols, D. Chen, L. You, Z. Chen, K. Wang, K. Wang, T.Z. Ward, Z. Gai, H.N. Lee, A.S. Sefat, V. Lauter, Z.-K. Liu, H.M. Christen, Epitaxial Growth of Intermetallic MnPt Films on Oxides and Large Exchange Bias, Adv. Mater. 28 (2016) 118–123, https://doi.org/10.1002/adma.201502606.
[8] M. Meinert, B. Büker, D. Graulich, M. Dunz, Large exchange bias in polycrystalline MnN/CoFe bilayers at room temperature, Phys. Rev. B 92 (2015) 144408, , https://doi.org/10.1103/PhysRevB.92.144408.
[9] S. Fukami, C. Zhang, S. DuttaGupta, A. Kurenkov, H. Ohno, Magnetization switching by spin–orbit torque in an antiferromagnet–ferromagnet bilayer system, Nat. Mater. 15 (2016) 535–541, https://doi.org/10.1038/nmat4566.
[10] N. Fontaíña Troitiño, B. Rivas-Murias, B. Rodríguez-González, V. Salgueiriño, Exchange Bias effect in CoO@$Fe_3O_4$ core–Shell octahedron-shaped nanoparticles, Chem. Mater. 26 (2014) 5566–5575, https://doi.org/10.1021/cm501951u.
[11] J.A. González, J.P. Andrés, R. López Antón, J.A. De Toro, P.S. Normile, P. Muñiz, J.M. Riveiro, J. Nogués, Maximizing Exchange Bias in Co/CoO Core/Shell Nanoparticles by Lattice Matching between the Shell and the Embedding Matrix, Chem. Mater. 29 (2017) 5200–5206, https://doi.org/10.1021/acs.chemmater.7b00868.
[12] J.M.D. Coey, M. Venkatesan, C.B. Fitzgerald, Donor impurity band exchange in dilute ferromagnetic oxides, Nat. Mater. 4 (2005) 173–179, https://doi.org/10.1038/nmat1310.
[13] M. Dolci, Y. Liu, X. Liu, C. Leuvrey, A. Derory, D. Begin, S. Begin-Colin, B.P. Pichon, Exploring exchange Bias coupling in $Fe_{3-\delta}O_4$@CoO core–shell nanoparticle 2D assemblies, Adv. Funct. Mater. 28 (2018) 1706957, , https://doi.org/10.1002/adfm.201706957.
[14] C. Park, R. Wu, P. Lu, H. Zhao, J. Yang, B. Zhang, W. Li, C. Yun, H. Wang, J.L. MacManus-Driscoll, S. Cho, Use of mesoscopic host matrix to induce ferrimagnetism in antiferromagnetic spinel oxide, Adv. Funct. Mater. 28 (2018) 1706220, , https://doi.org/10.1002/adfm.201706220.
[15] X. He, Y. Wang, N. Wu, A.N. Caruso, E. Vescovo, K.D. Belashchenko, P.A. Dowben, C. Binek, Robust isothermal electric control of exchange bias at room temperature, Nat. Mater. 9 (2010) 579–585, https://doi.org/10.1038/nmat2785.
[16] Y. Sun, J.-Z. Cong, Y.-S. Chai, L.-Q. Yan, Y.-L. Zhao, S.-G. Wang, W. Ning, Y.-H. Zhang, Giant exchange bias in a single-phase magnet with two magnetic sublattices, Appl. Phys. Lett. 102 (2013) 172406, , https://doi.org/10.1063/1.

4804179.
[17] X. Wang, X. Cheng, S. Gao, J. Song, K. Ruan, X. Li, Room temperature exchange bias in $SmFeO_3$ single crystal, J. Magn. Magn. Mater. 399 (2016) 170–174, https://doi.org/10.1016/j.jmmm.2015.09.074.
[18] S. Dong, Y. Yao, Y. Hou, Y. Liu, Y. Tang, X. Li, Dynamic properties of spin cluster glass and the exchange bias effect in $BiFeO_3$ nanocrystals, Nanotechnology 22 (385701) (2011), https://doi.org/10.1088/0957-4484/22/38/385701.
[19] H.L. Feng, P. Adler, M. Reehuis, W. Schnelle, P. Pattison, A. Hoser, C. Felser, M. Jansen, High-temperature ferrimagnetism with large coercivity and exchange bias in the partially ordered 3d/5d hexagonal perovskite $Ba_2Fe_{1.12}Os_{0.88}O_6$, Chem. Mater. 29 (2017) 886–895, https://doi.org/10.1021/acs.chemmater.6b04983.
[20] A.K. Nayak, M. Nicklas, S. Chadov, P. Khuntia, C. Shekhar, A. Kalache, M. Baenitz, Y. Skourski, V.K. Guduru, A. Puri, U. Zeitler, J.M.D. Coey, C. Felser, Design of compensated ferrimagnetic Heusler alloys for giant tunable exchange bias, Nat. Mater. 14 (2015) 679–684, https://doi.org/10.1038/nmat4248.
[21] Y. Huang, G. Wang, S. Sun, J. Wang, R. Peng, Y. Lin, X. Zhai, Z. Fu, Y. Lu, Observation of exchange anisotropy in single-phase layer-structured oxides with long periods, Sci. Rep. 5 (2015) 15261, https://doi.org/10.1038/srep15261.
[22] G. Wang, Y. Huang, S. Sun, J. Wang, R. Peng, Y. Lu, X. Tan, Layer effects on the magnetic behaviors of aurivillius compounds $Bi_{n+1}Fe_{n-3}Ti_3O_{3n+1}$ (n = 6, 7, 8, 9), J. Am. Ceram. Soc. 99 (2016) 1318–1323, https://doi.org/10.1111/jace.14108.
[23] G. Wang, H. Yang, J. Wang, S. Sun, Z. Fu, X. Zhai, R. Peng, R.J. Knize, Y. Lu, Engineering the exchange bias and bias temperature by modulating the spin glassy state in single phase $Bi_9Fe_5Ti_3O_{27}$, Nanoscale. 9 (2017) 8305–8313, https://doi.org/10.1039/C7NR02156A.
[24] J.-B. Li, Y.-P. Huang, H.-B. Jin, G.-H. Rao, J.-K. Liang, Inhomogeneous structure and magnetic properties of aurivillius ceramics $Bi_4Bi_{n-3}Ti_3Fe_{n-3}O_{3n+3}$, J. Am. Ceram. Soc. 96 (2013) 3920–3925, https://doi.org/10.1111/jace.12614.
[25] S. Horiuchi, K. Muramatsu, M. Shimazu, Intergrowth in complex bismuth oxides, $Bi_2CaNa_{n-2}Nb_nO_{3n+3}$ (n=5∼8), revealed by 1-MV high-resolution electron microscopy, J. Solid State Chem. 34 (1980) 51–57, https://doi.org/10.1016/0022-4596(80)90402-8.
[26] K. Muramatsu, M. Shimazu, J. Tanaka, S. Horiuchi, High n-value phases in the complex bismuth oxides with layered structure, $Bi_2CaNa_{n-2}Nb_nO_{3n+3}$, J. Solid State Chem. 36 (1981) 179–182, https://doi.org/10.1016/0022-4596(81)90154-7.
[27] G. Kresse, J. Furthmüller, Efficient iterative schemes for ab initio total-energy calculations using a plane-wave basis set, Phys. Rev. B 54 (1996) 11169–11186, https://doi.org/10.1103/PhysRevB.54.11169.
[28] J.P. Perdew, K. Burke, M. Ernzerhof, Generalized gradient approximation made simple, Phys. Rev. Lett. 77 (1996) 3865–3868, https://doi.org/10.1103/PhysRevLett.77.3865.
[29] S.L. Dudarev, G.A. Botton, S.Y. Savrasov, C.J. Humphreys, A.P. Sutton, Electron-energy-loss spectra and the structural stability of nickel oxide: an LSDA+U study, Phys. Rev. B 57 (1998) 1505–1509, https://doi.org/10.1103/PhysRevB.57.1505.
[30] L. Wang, T. Maxisch, G. Ceder, Oxidation energies of transition metal oxides within the GGA+ U framework, Phys. Rev. B 73 (2006) 195107, , https://doi.org/10.1103/PhysRevB.73.195107.
[31] J. Yang, W. Tong, Z. Liu, X.B. Zhu, J.M. Dai, W.H. Song, Z.R. Yang, Y.P. Sun, Structural, magnetic, and EPR studies of the Aurivillius phase $Bi_6Fe_2Ti_3O_{18}$ and $Bi_6FeCrTi_3O_{18}$, Phys. Rev. B 86 (2012), https://doi.org/10.1103/PhysRevB.86.104410.
[32] A. Srinivas, D.-W. Kim, K.S. Hong, S.V. Suryanarayana, Study of magnetic and magnetoelectric measurements in bismuth iron titanate ceramic—$Bi_8Fe_4Ti_3O_{24}$, Mater. Res. Bull. 39 (2004) 55–61, https://doi.org/10.1016/j.materresbull.2003.09.028.
[33] A.Y. Birenbaum, C. Ederer, Potentially multiferroic Aurivillius phase $Bi_5FeTi_3O_{15}$: cation site preference, electric polarization, and magnetic coupling from first principles, Phys. Rev. B 90 (2014) 214109.
[34] S. Sun, Y. Huang, G. Wang, J. Wang, R. Peng, Z. Fu, X. Zhai, Xiangyu Mao, X. Chen, Y. Lu, Room-temperature multiferroic responses arising from 1D phase modulation in correlated Aurivillius-type layer structures, J. Phys. D Appl. Phys. 49 (2016) 125005, , https://doi.org/10.1088/0022-3727/49/12/125005.
[35] N.C. Hyatt, J.A. Hriljac, T.P. Comyn, Cation disorder in $Bi_2Ln_2Ti_3O_{12}$ Aurivillius phases (Ln = La, Pr, Nd and Sm), Mater. Res. Bull. 38 (2003) 837–846, https://doi.org/10.1016/S0025-5408(03)00032-1.
[36] J. Dho, N.H. Hur, Thickness dependence of perpendicular magnetic anisotropy in $La_{0.7}Sr_{0.3}MnO_3$ films on $LaAlO_3$, J. Magn. Magn. Mater. 318 (2007) 23–27, https://doi.org/10.1016/j.jmmm.2007.04.038.
[37] S. Das, A. Herklotz, E. Pippel, E.J. Guo, D. Rata, K. Dörr, Strain dependence of antiferromagnetic interface coupling in $La_{0.7}Sr_{0.3}MnO_3/SrRuO_3$ superlattices, Phys. Rev. B 91 (2015) 134405, , https://doi.org/10.1103/PhysRevB.91.134405.
[38] R. Galceran, L. López-Mir, B. Bozzo, J. Cisneros-Fernández, J. Santiso, L. Balcells, C. Frontera, B. Martínez, Strain-induced perpendicular magnetic anisotropy in $La_2CoMnO_{6-\varepsilon}$ thin films and its dependence on film thickness, Phys. Rev. B 93 (2016), https://doi.org/10.1103/PhysRevB.93.144417.
[39] B. Chen, H. Xu, C. Ma, S. Mattauch, D. Lan, F. Jin, Z. Guo, S. Wan, P. Chen, G. Gao, et al., All-oxide–based synthetic antiferromagnets exhibiting layer-resolved magnetization reversal, Science 357 (2017) 191–194.
[40] F.K. Lotgering, Topotactical reactions with ferrimagnetic oxides having hexagonal crystal structures—I, J. Inorg. Nucl. Chem. 9 (1959) 113–123, https://doi.org/10.1016/0022-1902(59)80070-1.
[41] E. Jartych, T. Pikula, M. Mazurek, A. Lisinska-Czekaj, D. Czekaj, K. Gaska, J. Przewoznik, C. Kapusta, Z. Surowiec, Antiferromagnetic spin glass-like behavior in sintered multiferroic Aurivillius $Bi_{m+1}Ti_3Fe_{m-3}O_{3m+3}$ compounds, J. Magn. Magn. Mater. 342 (2013) 27–34, https://doi.org/10.1016/j.jmmm.2013.04.046.
[42] S. Thomas, G. Pookat, S.S. Nair, M. Daniel, B. Dymerska, A. Liebig, S.H. Al-Harthi, R.V. Ramanujan, M.R. Anantharaman, J. Fidler, M. Albrecht, Exchange bias effect in partially oxidized amorphous Fe–Ni–B based metallic glass nanostructures, J. Phys. Condens. Matter. 24 (2012) 256004, , https://doi.org/10.1088/0953-8984/24/25/256004.
[43] C.M. Soukoulis, K. Levin, G.S. Grest, Reversibility and irreversibility in spin-glasses: the free-energy surface, Phys. Rev. Lett. 48 (1982) 1756–1759, https://doi.org/10.1103/PhysRevLett.48.1756.
[44] S. Vijayanand, M.B. Mahajan, H.S. Potdar, P.A. Joy, Magnetic characteristics of nanocrystalline multiferroic $BiFeO_3$ at low temperatures, Phys. Rev. B 80 (2009), https://doi.org/10.1103/PhysRevB.80.064423.
[45] S. Sun, Z. Chen, G. Wang, X. Geng, Z. Xiao, Z. Sun, Z. Sun, R. Peng, Y. Lu, Nanoscale Structural Modulation and Low-temperature Magnetic Response in Mixed-layer Aurivillius-type Oxides, Sci. Rep. 8 (2018), https://doi.org/10.1038/s41598-018-19448-1.